Support Information

Performance Advancements in P-Type TaFeSb-Based Thermoelectric Materials through Composition and Composite Optimizations

*Raana Hatami Naderloo,[a] Ruben Bueno Villoro,[b] Dominique Alexander Mattlat,[b] Pingjun Ying,[a] Shaowei Song,[c] Samaneh Bayesteh,[a] Kornelius Nielsch,[a] Christina Scheu,[b] Zhifeng Ren,[c] Hangtian Zhu,[*c,d] Siyuan Zhang [*b] and Ran He[*a]*

[a]R. Hatami Naderloo, P. Ying, S. Bayesteh, K. Nielsch, R. He.
Leibnitz Institute for Solid State and Materials Research Dresden e.V.
(IFW-Dresden)
01069 Dresden, Germany
E-mail: r.he@ifw-dresden.de

[b]R. Bueno Villoro, D. A. Mattlat, C. Scheu, S. Zhang.
Max-Planck-Institute für Eisenforschung GmbH
40237 Duesseldorf, Germany
E-mail: siyuan.zhang@mpie.de

[c]S. Song, Z. Ren, H. Zhu.
Department of Physics and Texas Center for Superconductivity
University of Houston
TX 77204 Houston, U.S.A.

[d]H. Zhu
Beijing National Laboratory for Condensed Matter Physics, Institute of Physics, Chinese Academy of Sciences
Beijing 100190, China
E-mail: htzhu@iphy.ac.cn

Keywords: *p*-type TaFeSb, half-Heuslers, composite, thermoelectric materials, average *zT,* efficiency

i) Price contrast among elements

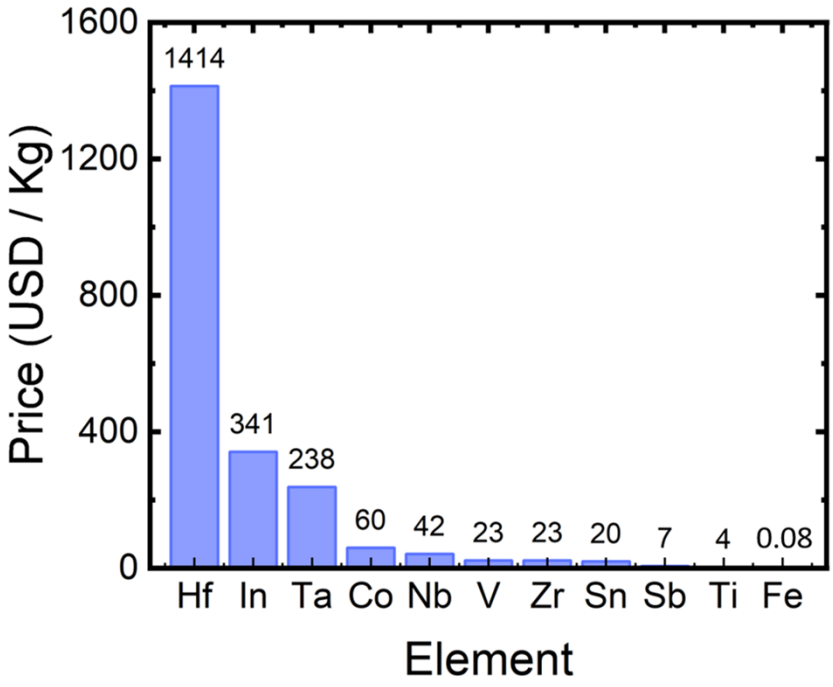

Fig. S1 Element's price in USD per Kg. The prices have been checked on this website: *Chemical elements by market price (leonland.de)*. Chemical elements by market price (leonland.de)Chemical elements by market price (leonland.de)

ii) Iterative optimization approach for (Ta,Nb,V,Ti)FeSb-based half-Heusler compounds

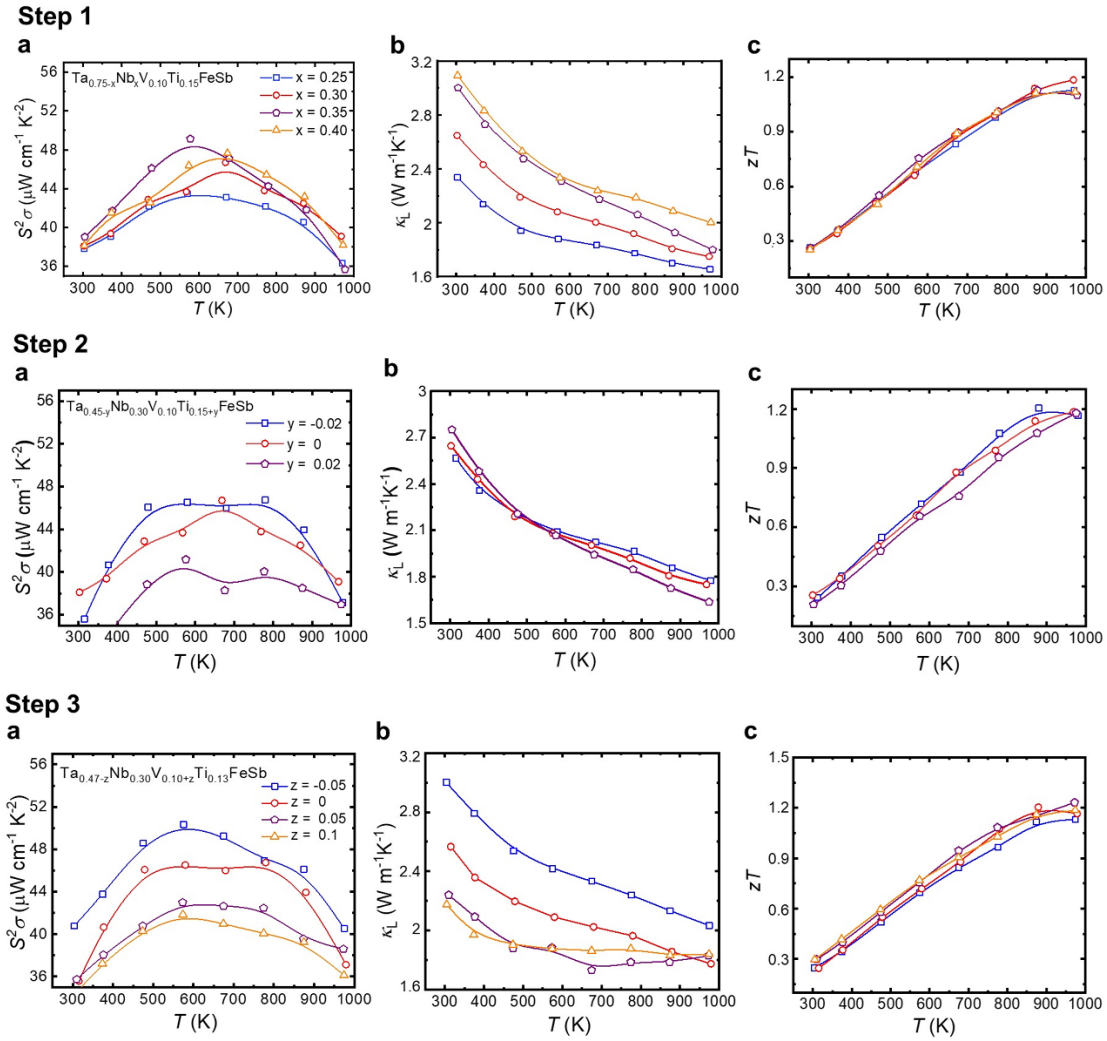

Fig. S2 The step-wise optimization procedure of (Ta,Nb,V,Ti)FeSb-based half-Heusler compound. The optimization has been done spanning from room temperature to 973 K in three steps.

iii) XRD patterns of $Ta_{0.42}Nb_{0.3}V_{0.15}Ti_{0.13}FeSb$-$(InSb)_{\delta}$ half-Heusler composites

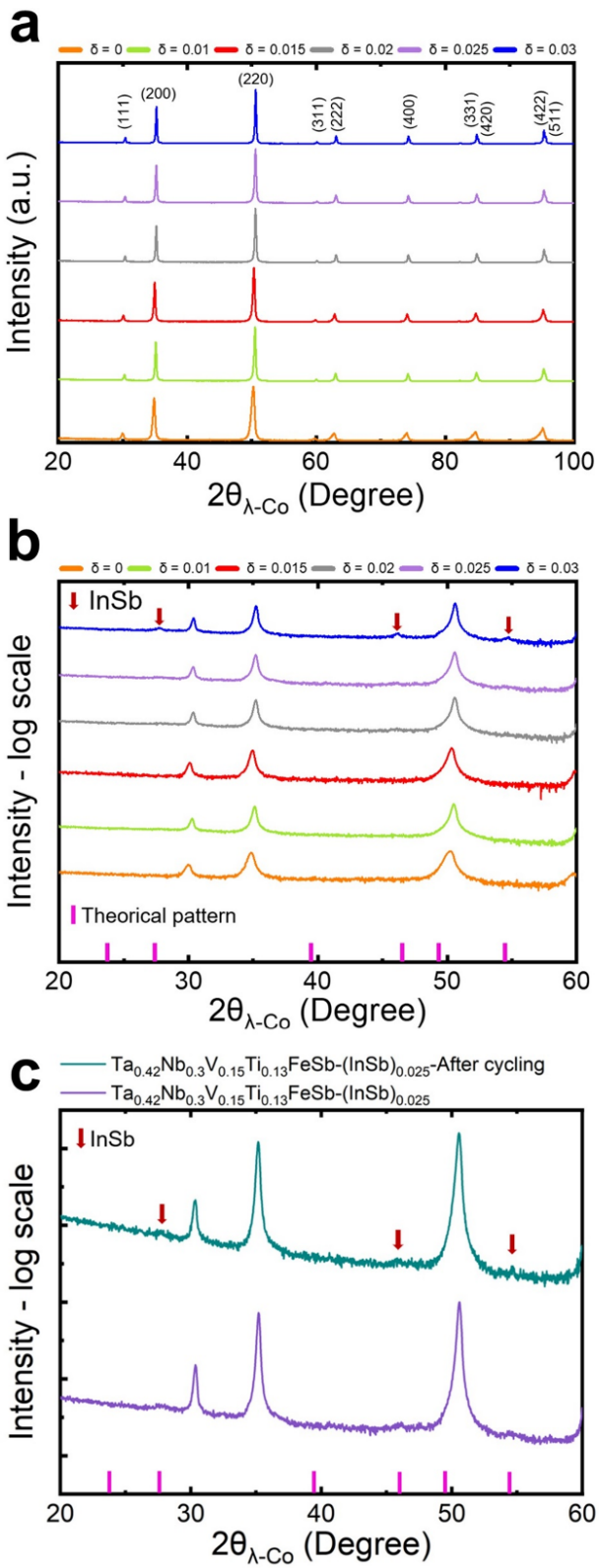

Fig. S3 XRD patterns of $Ta_{0.42}Nb_{0.3}V_{0.15}Ti_{0.13}FeSb$-$(InSb)_{\delta}$ (δ = 0, 0.01, 0.015, 0.02, 0.025 and 0.03) composites. a) complete view and b) zoomed-in version with the intensity in log scale to showcase the secondary phases, c) zoomed-in XRD patterns of $Ta_{0.42}Nb_{0.3}V_{0.15}Ti_{0.13}FeSb$-$(InSb)_{0.025}$ with the intensity in log scale to showcase the secondary phases before and after 6 times cycling. Pink solid lines are theoretical pattern of InSb. [1]

iv) Verifying the consistency of thermoelectric properties for $Ta_{0.42}Nb_{0.3}V_{0.15}Ti_{0.13}FeSb$-$(InSb)_{0.015}$

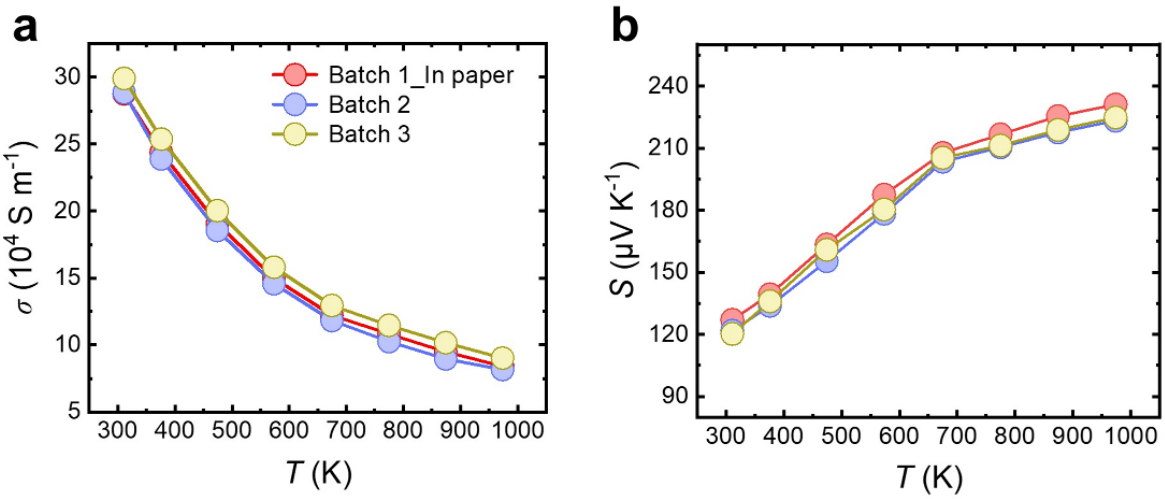

Fig. S4 Consistency of thermoelectric properties for $Ta_{0.42}Nb_{0.3}V_{0.15}Ti_{0.13}FeSb$-$(InSb)_{0.015}$. Temperature dependent a) electrical conductivity and b) Seebeck coefficient of $Ta_{0.42}Nb_{0.3}V_{0.15}Ti_{0.13}FeSb$-$(InSb)_{0.015}$ among three different batches.

v) Assessing electrical properties during cycling up to 973 K for $Ta_{0.42}Nb_{0.3}V_{0.15}Ti_{0.13}FeSb$-$(InSb)_{0.015}$

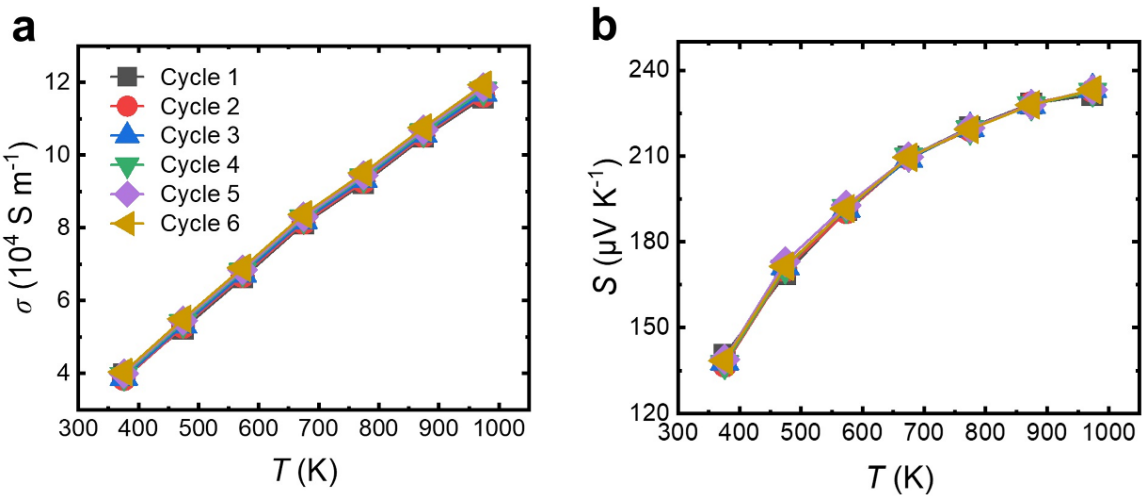

Fig. S5 Electrical properties during cycling for $Ta_{0.42}Nb_{0.3}V_{0.15}Ti_{0.13}FeSb$-$(InSb)_{0.015}$. Temperature dependent of a) electrical conductivity and b) relative Seebeck coefficient of $Ta_{0.42}Nb_{0.3}V_{0.15}Ti_{0.13}FeSb$-$(InSb)_{0.015}$ upon cycling up to 973 K for 6 times.

vi) Temperature-dependent electrical conductivity across all samples

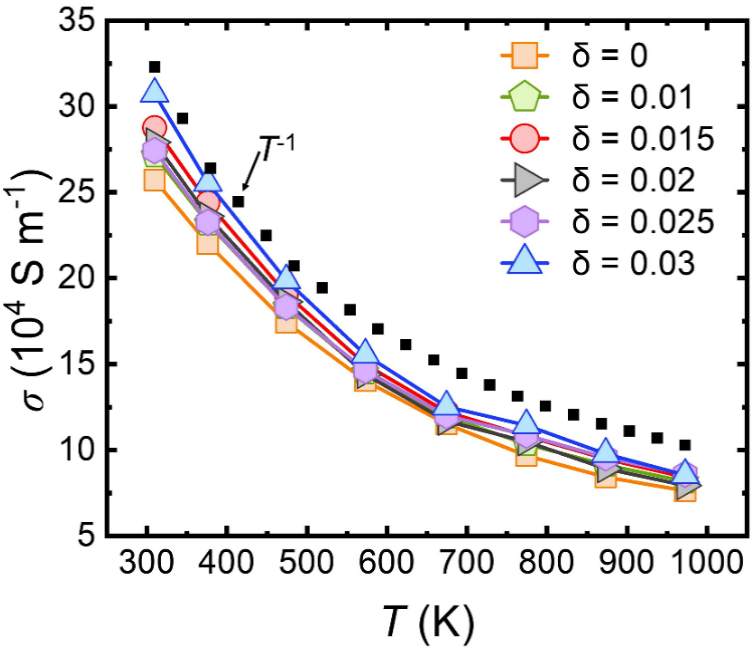

Fig. S6 Temperature-dependent electrical conductivity $Ta_{0.42}Nb_{0.3}V_{0.15}Ti_{0.13}FeSb$-$(InSb)_{\delta}$ (δ = 0, 0.01, 0.015, 0.02, 0.025 and 0.03). The power-law curve shown as a black dotted plot.

vii) Comparison of Seebeck coefficients among three batches of $Ta_{0.42}Nb_{0.3}V_{0.15}Ti_{0.13}FeSb$ and $Ta_{0.42}Nb_{0.3}V_{0.15}Ti_{0.13}FeSb$-$(InSb)_{0.015}$

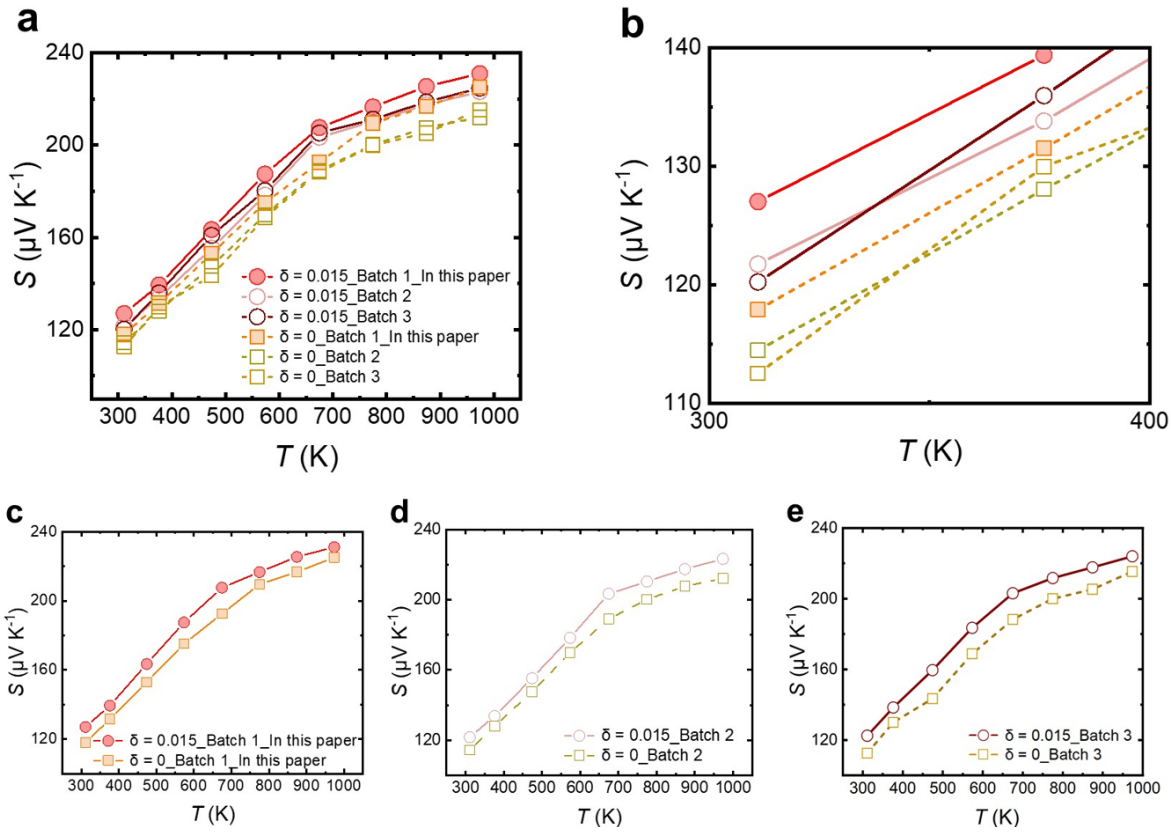

Fig. S7 Temperature dependent Seebeck coefficient of $Ta_{0.42}Nb_{0.3}V_{0.15}Ti_{0.13}FeSb$-$(InSb)_{\delta}$ materials (δ = 0 and 0.015). a) comparison among three different batches, b) zoom-in display of a from 300 K to 400 K. Separated comparison of c) batch_1, d) batch_2, and e) batch_3.

viii) The room temperature Seebeck coefficient, analyzed as a function of Hall concentration and m^*_{DOS}, drawing inspiration from the Pisarenko Formula

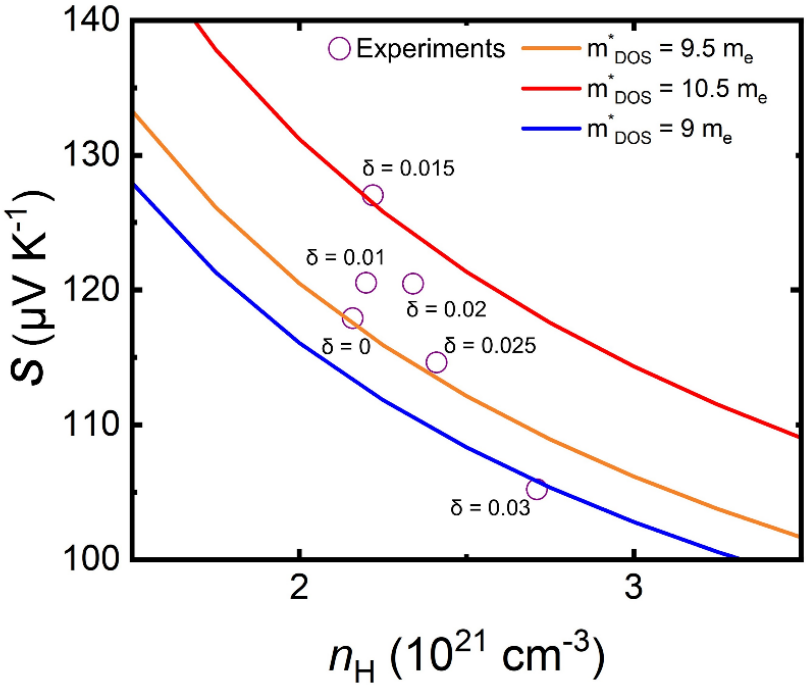

Fig. S8 Seebeck coefficient *vs.* Hall concentration at 300 K. The solid lines are Pisarenko plots with different density-of-state effective masses (m^*_{DOS}). The Violet circle shows the experimental Seebeck coefficient for $Ta_{0.42}Nb_{0.3}V_{0.15}Ti_{0.13}FeSb$-$(InSb)_\delta$ alloys at 300 K.

ix) Electrical properties of $Ta_{0.42}Nb_{0.3}V_{0.15}Ti_{0.13}FeSb$-$(InSb)_{\delta}$ (δ = 0, 0.01, 0.015, 0.02, 0.025 and 0.03) composites

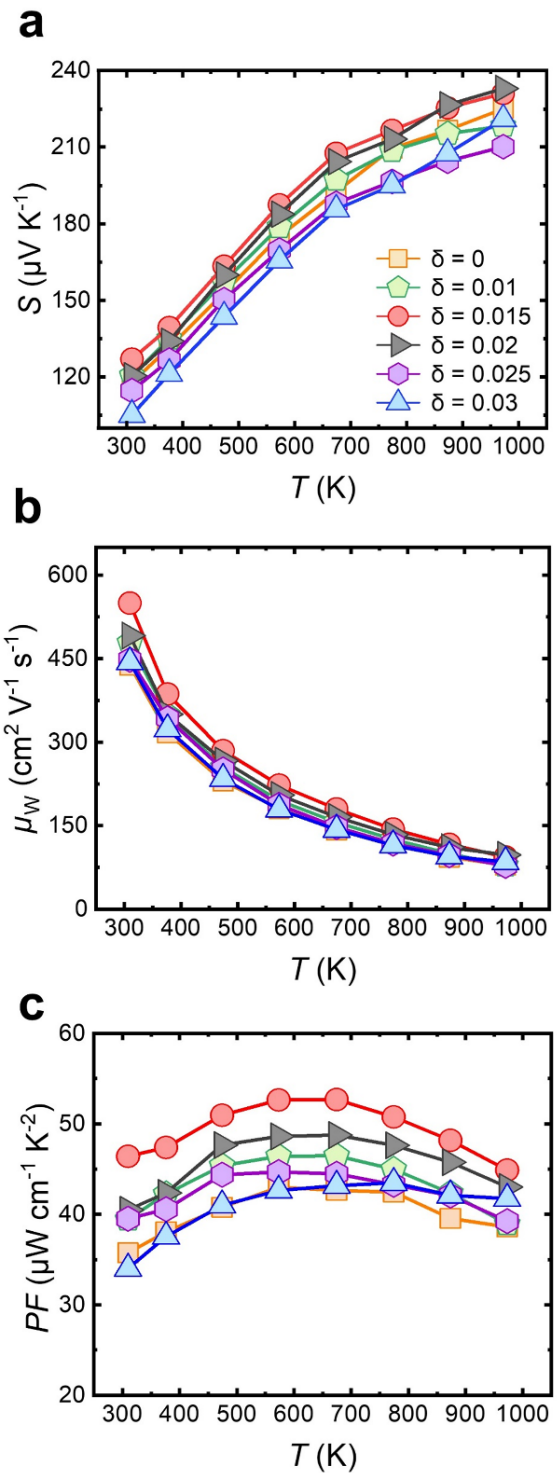

Fig. S9 Electrical properties of $Ta_{0.42}Nb_{0.3}V_{0.15}Ti_{0.13}FeSb$-$(InSb)_{\delta}$ (δ = 0, 0.01, 0.015, 0.02, 0.025 and 0.03) composites. Temperature-dependent of a) Seebeck coefficient, b) weighted mobility, c) power factor.

x) Schematics of the mechanisms of modified GB in modifying the electrons transport

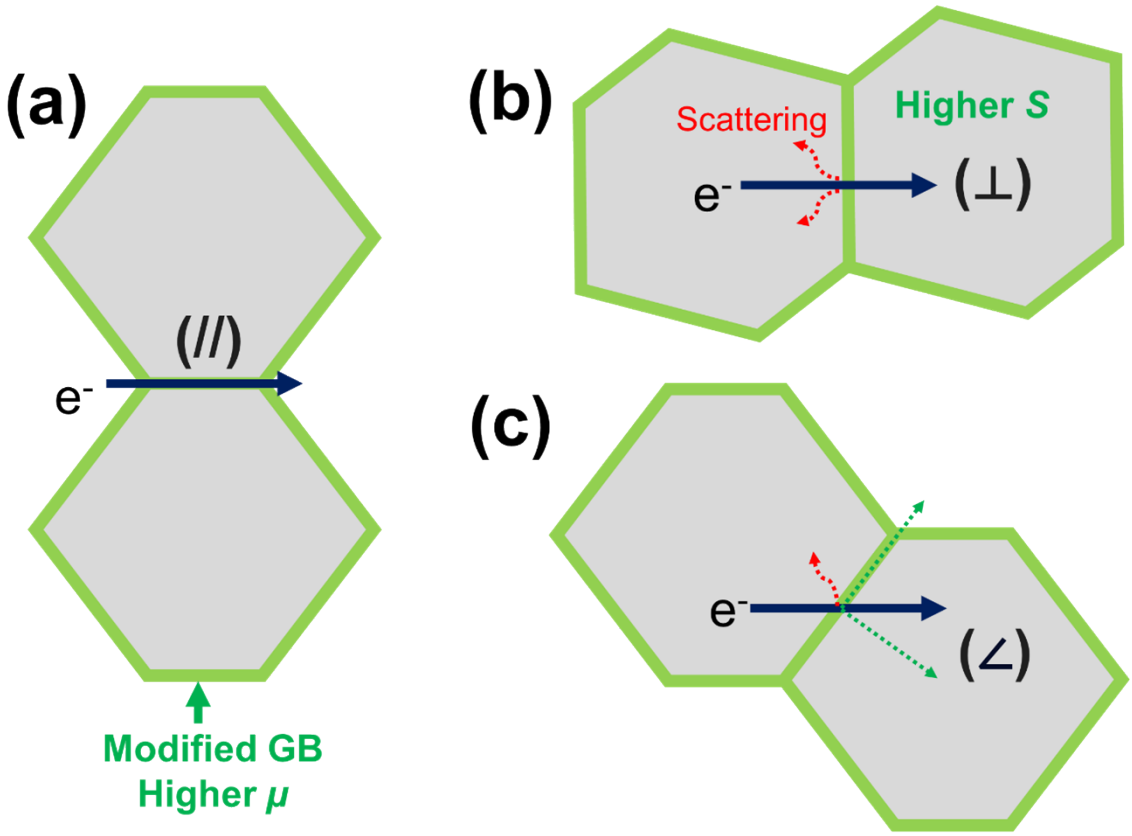

Fig. S10. Schematic illustration of the mechanisms by which modified grain boundaries influence the electronic transport properties of $Ta_{0.42}Nb_{0.3}V_{0.15}Ti_{0.13}FeSb\_InSb$. Depending on the incident direction of charge carriers, two distinct effects may arise: (a) when charge carriers travel parallel to the grain boundaries, mobility is enhanced; (b) when charge carriers encounter the grain boundaries perpendicularly, the Seebeck coefficient is higher due to increased scattering. In realistic scenarios (c), charge carriers approach the grain boundaries at random angles, resulting in a combination of both effects.

xi) Integrated analysis of SEM images and elemental mapping via EDX and EBSD

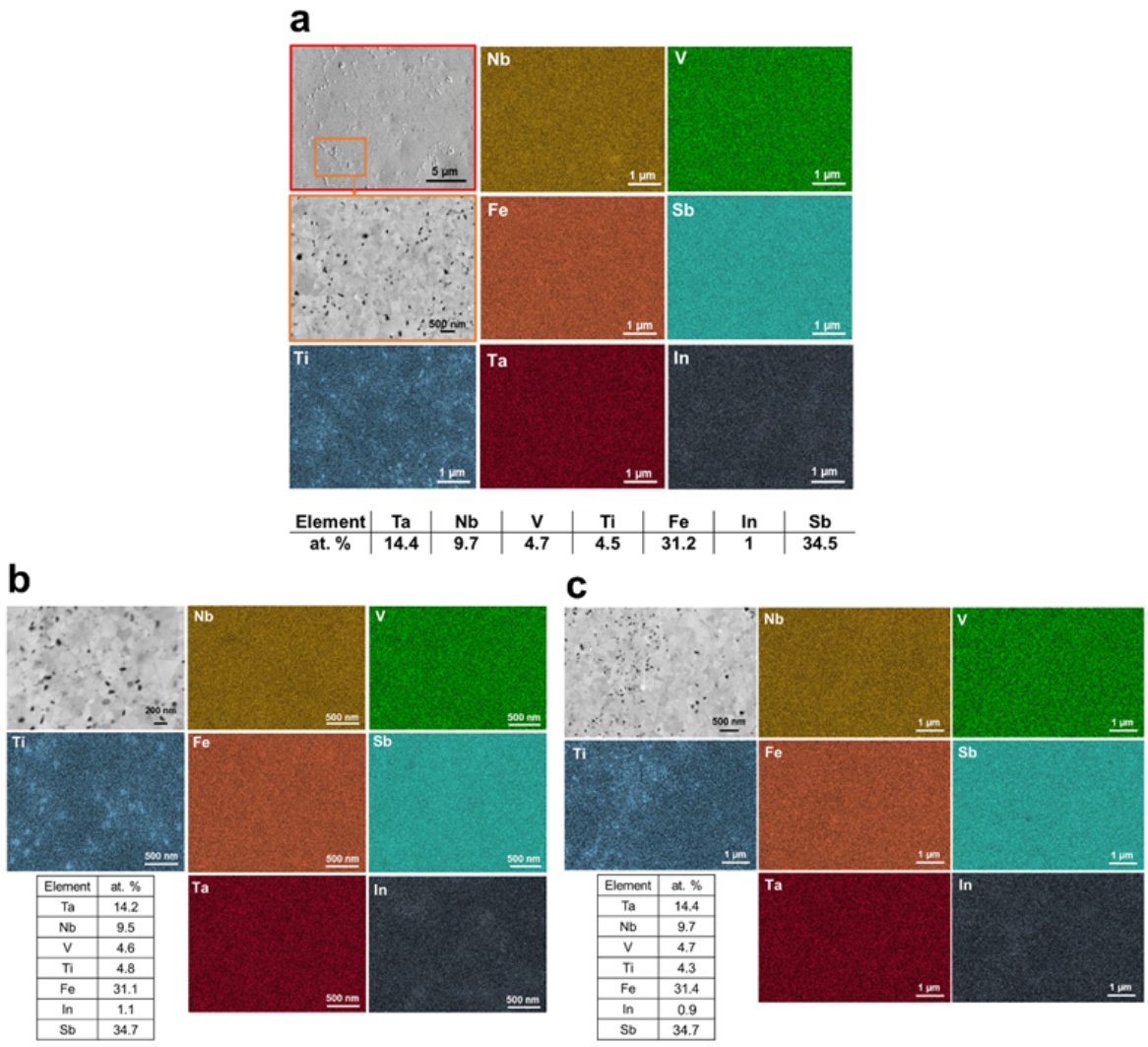

Element	Ta	Nb	V	Ti	Fe	In	Sb
at. %	14.4	9.7	4.7	4.5	31.2	1	34.5

Element	at. %
Ta	14.2
Nb	9.5
V	4.6
Ti	4.8
Fe	31.1
In	1.1
Sb	34.7

Element	at. %
Ta	14.4
Nb	9.7
V	4.7
Ti	4.3
Fe	31.4
In	0.9
Sb	34.7

Fig. S11 Integrated analysis of SEM images and elemental mapping via EDX for $Ta_{0.42}Nb_{0.3}V_{0.15}Ti_{0.13}FeSb\text{-}(InSb)_{0.015}$.

Table S1. Elemental quantification of $Ta_{0.42}Nb_{0.3}V_{0.15}Ti_{0.13}FeSb$-$(InSb)_{0.015}$ by EDX.

Elements	Ta	Nb	V	Ti	Fe	Sb	In
Position 1	14.4	9.7	4.7	4.5	31.2	34.5	1
Position 2	14.2	9.5	4.6	4.8	31.1	34.7	1.1
Position 3	14.4	9.7	4.7	4.3	31.4	34.7	0.9
Nominal	13.9	9.9	4.9	4.3	33.0	33.5	0.5

xii) Evaluating the presence of TiO_x

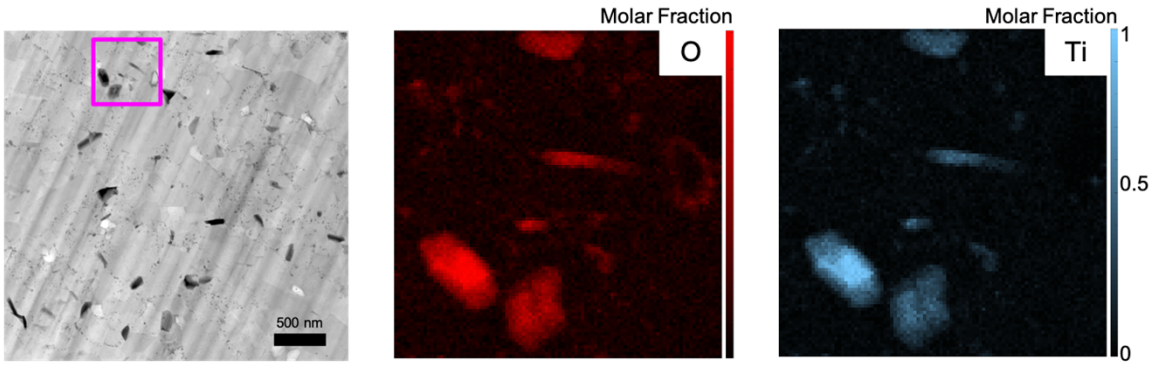

Fig. S12 HAADF-STEM image of the $Ta_{0.42}Nb_{0.3}V_{0.15}Ti_{0.13}FeSb$-$(InSb)_{0.015}$ sample. Highlighting the distribution of TiO_x precipitates in the EDX maps of O and Ti.

xiii) Complete thermal properties and *zT* across samples with varied InSb content

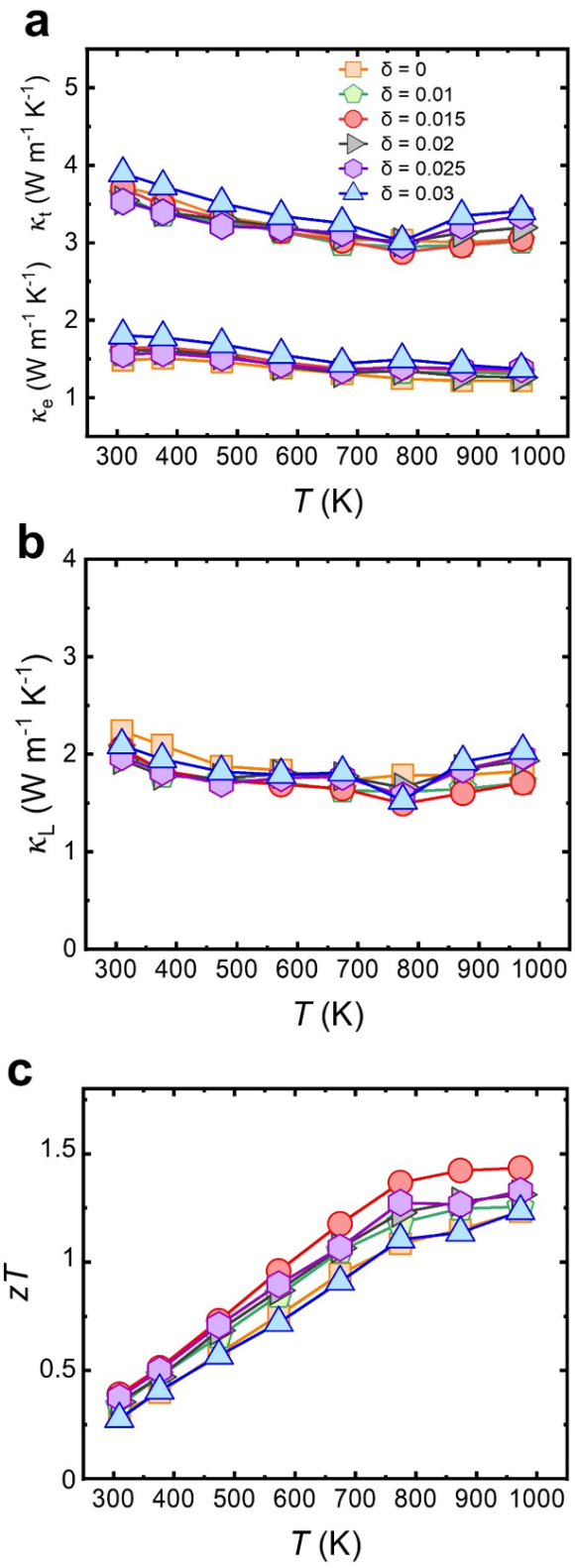

Fig. S13 Complete thermal properties and *zT* of $Ta_{0.42}Nb_{0.3}V_{0.15}Ti_{0.13}FeSb$-$(InSb)_{\delta}$ (δ = 0, 0.01, 0.015, 0.02, 0.025 and 0.03) composites. Temperature-dependent a) total thermal conductivity and electronical thermal conductivity, b) lattice thermal conductivity, c) *zT*

xiv) Temperature dependent specific heat capacity (C_p)

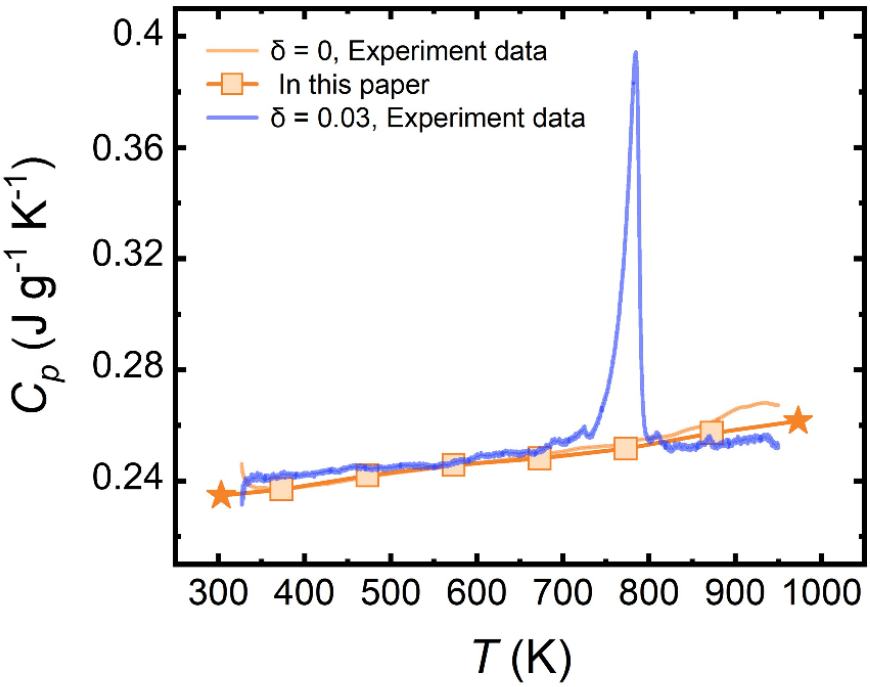

Fig. S14 Temperature-dependent specific heat capacity (C_p) of $Ta_{0.42}Nb_{0.3}V_{0.15}Ti_{0.13}FeSb$ and $Ta_{0.42}Nb_{0.3}V_{0.15}Ti_{0.13}FeSb$-$(InSb)_{0.03}$. The curves are measurement results, the squares and stars are used to calculate the thermal conductivity at the corresponding temperatures. The stars (at 300 K and 973 K) are linear extrapolations based on the squares. The endothermic peak of δ = 0.03 sample corresponds to the melting of InSb-related phase.

The C_p values for the δ = 0 and δ = 0.03 specimens were measured, while those for other InSb-containing samples were not. This approach is justified as the specific heat capacities of the two end compositions were found to be nearly identical, except for deviations around 773 K due to a phase transition. Additionally, the maximum InSb content in the samples is less than 2 at% (calculated as 2/3×3%), resulting in a negligible contribution to the total heat capacity. Thus, the trace amount of InSb is unlikely to significantly affect the overall heat capacity, validating the use of a single value across all samples.

It is worth noting that determining C_p values at 300 K and 973 K experimentally poses challenges. At 973 K, the measurement approaches the device's operational limit, while at 300 K, achieving thermal equilibrium introduces significant errors. Therefore, C_p values at these temperatures were linearly extrapolated from the measured data between 373 K and 873 K, as indicated by the stars in the figure.

Reference

1. K. C. Hewitt, L. Y. Beaulieu, J. R. Dahn**,** *Electrochem Soc,* 2001*,* **148**, A402.